CHINESE OPTICS LETTERS

Vol. 20, No. 12 | December 2022

High-performance millimeter-scale silicon grating emitters for beam steering applications

Ze Chen (陈 泽)[1,2], Haibin Lü (吕海斌)[3], Yanfeng Chen (陈延峰)[1,2*], and Xiaoping Liu (刘晓平)[3**]

[1] National Laboratory of Solid State Microstructures and College of Engineering and Applied Sciences, Nanjing University, Nanjing 210093, China

[2] Collaborative Innovation Center of Advanced Microstructures, Nanjing University, Nanjing 210093, China

[3] School of Physical Science and Technology, ShanghaiTech University, Shanghai 201210, China

*Corresponding author: yfchen@nju.edu.cn

**Corresponding author: liuxp1@shanghaitech.edu.cn

Received February 18, 2022 | Accepted June 17, 2022 | Posted Online September 28, 2022

A 2-mm-long silicon-on-insulator grating emitter with a narrow angular full width at half-maximum (FWHM) and a high sideband suppression ratio (SSR) is proposed and designed. It consists of a Si_3N_4/Si grating with an approximate Gaussian emission profile along the grating length, which aims to reduce the sidelobe intensity of the scanning light in the far-field, thereby improving the resolution of the longitudinal steering resolution of the light detection and ranging (lidar). Numerical analysis shows that the angular FWHM of the emitted beam could be as low as 0.026° for a grating length of 2.247 mm and the input TE-like waveguide mode at 1550 nm, and the SSR could be more than 32.622 dB. Moreover, this Si_3N_4/Si grating exhibits a favorable fabrication error tolerance when considering the width and length variation of the Si_3N_4 overlayer in practice. Our design offers a promising platform for realizing integrated optical phased arrays for the long-distance solid-state lidar.

Keywords: grating emitter; coupled-mode theory; genetic algorithm.

DOI: 10.3788/COL202220.121301

1. Introduction

With the rise of autonomous vehicles[1–3] and unmanned drones[4], light detection and ranging (lidar) has become an indispensable device for them. So far, the mechanical lidar[5] is still one of the most mature solutions, but its high cost and difficult assembly have plagued researchers. Besides, the short detection distance limits the wide application of flash lidars[6]. The integrated on-chip silicon (Si) optical phased array (OPA)[7–11], as an advanced solid-state beam steering device, can overcome the above defects and has gained significant interest for its energy saving and miniaturization. In application, the grating-emitter-based OPA is considered a viable candidate to achieve two-dimensional (2D) optical steering, i.e., phase steering in one direction and wavelength steering in the other direction. For phase steering, the OPA with a pitch close to a half-wavelength along the lateral direction is constructed to realize a wide beam steering range with low crosstalk, which is usually built upon metamaterial waveguides[12,13], corrugated waveguides[14], nano-structured Si waveguide arrays[15], etc. Notably, an OPA with a phase mismatched unequal width waveguide distribution has been applied, implementing a steering range of 110° and a maximum peak power of 720 mW[16]. Wavelength steering is often enabled by the grating dispersion when the wavelength of the input laser light is scanned. A macroscopic emitting aperture with its size of > 1 mm is typically required for ranging distances of interest for autonomous vehicles[17] because a larger aperture would generally enable a narrower width of the main beam lobe and thus a high angular imaging resolution. The Si waveguide grating with shallow etching is one possible approach to realizing long-length emitting for its weak emission rate[18]. However, in practice, they are challenging to fabricate. A more promising approach of integrating a Si nitride (Si_3N_4) overlayer on a Si waveguide has gained significant interest because of its low nonlinearity, broad transparency range, low propagation loss, and low index contrast characteristics[4]. On this basis, several surface gratings with novel structures, such as strip-line grating[19] and fishbone grating[20], have been realized in the modulation of the emission profile and the improvement of radiation beam quality. In addition, the downward radiant power of the grating always introduces destructive interference, which reduces the performance of the grating emitter. An effective approach of dual-layer grating misalignment has been proposed, consequently achieving more than 95% unidirectional radiation[21].

In this Letter, we propose a Si_3N_4/Si grating emitter structure with a specific variation in widths and duty cycles of Si_3N_4 overlayers. This structure provides an approximate Gaussian emission profile and long effective coupling length of 2.247 mm. The design is mainly centered around two targets: (1) to increase the far-field sideband suppression ratio (SSR), thus reducing the interference of the scanning light sidelobes in the far-field to the steering detection, which is realized by constructing the Gaussian near-field emission profile; (2) to increase the steering accuracy, which is directly governed by the angular full width at half-maximum (FWHM) beamwidth related to the effective grating length. The coupled-mode theory (CMT) is employed to analyze the coupling between the guided mode and radiation mode. In addition, a genetic algorithm (GA)[22–24] drives the coupled-mode model to search a large parameter space containing the two geometric freedoms of Si_3N_4 overlayers (with fixed height) to produce the large-scale approximate Gaussian emission profile on the grating surface. Our theoretical investigation suggests that when the working wavelength is 1550 nm, the designed grating emitter can obtain a far-field angular FWHM beamwidth of less than 0.026° and an SSR of larger than 32.622 dB. In addition, the proposed grating emitter can realize longitudinal beam steering of 3.94° by wavelength tuning within the wavelength range of 1530–1570 nm. Our design here provides a practical and feasible approach for beam steering, shedding light on the possibilities of realizing high-performance solid-state lidars with a high signal-to-noise ratio (SNR) and detection accuracy.

2. Theory and Design

Purely numerical methods such as finite difference time domain (FDTD) are theoretically feasible for the grating design. However, accurate calculation results can only be obtained by the ultra-high-precision meshing of the millimeter (mm)-length rectangular structure, which undoubtedly consumes a significant amount of computing resources. By contrast, the CMT avoids the tedious meshing progress and can give quantitative predictions of the coupling between the guided mode and the radiation mode and a physical understanding of grating radiation. In the coupled-mode model employed here, by modulating the widths and duty cycles of Si_3N_4 overlayers, we can precisely control the coupling between the guided mode and radiation mode. In prior studies, radiation modes can be constructed in relatively simple forms for 2D slab waveguides[25] and optical fibers[26]. They cannot apply to our design of the Si_3N_4/Si grating emitter with a rectangular structure. We adopt the semi-analytical method proposed by Poulton[27] to construct fully 3D radiation modes of the ideal rectangular Si waveguide (see Appendix A for details), where the radiation modes are deduced from the response of the waveguide to an incoming extended field with a given symmetry and polarization to calculate power density functions of the radiation modes more explicitly and conveniently.

Shown schematically in Fig. 1, the customized grating is designed on a Si-on-insulator (SOI) platform. The Si waveguide has a height of 220 nm and a width W_{Si} of 500 nm. A Si_3N_4 overlayer with a height h_0 of 50 nm is deposited above the Si waveguide with SiO_2 cladding. The 2.247 mm grating contains 2500 grating periods totally with a period Λ of 899.07 nm. The coupling between the guided mode and the radiation mode is constrained by the (quasi-)phase matching condition, and the radiation field consequently emerges at an angle of 30° (referenced to the grating facet normal). As a traveling wave with a fixed radiation angle, the radiation field has a planar phase front. In practice, 2500 independently parametrized Si_3N_4 overlayers undoubtedly increase the difficulty of actual fabrication and reduce the robustness of the device. An effective optimization strategy is proposed here by (1) grouping a series of 25 neighboring grating periods as an optimization group, where the widths and duty cycles of the Si_3N_4 overlayers are set to be identical; (2) constructing two fitting functions g_1 and g_2, representing, respectively, the mapping relations from the group order S = 1–100 to the common widths and duty cycles of the Si_3N_4 overlayers in each group, to reduce the number of optimal variables. In particular, g_1 represents the percentage of the Si_3N_4 overlayer width to the Si core width. The fitting functions g_1 and g_2 can be expressed as

$$\begin{cases} g_1(S) = \sum_{j=0}^{40} a_j[(S-50)/a_{41}]^j + a_{42}e^{-(S-a_{43})^2/a_{44}} \\ g_2(S) = \sum_{j=0}^{40} b_i[(S-50)/b_{41}]^j + b_{42}e^{-(S-b_{43})^2/b_{44}} \end{cases}, \quad (1)$$

where a_j and b_j ($j = 0, 1, \ldots, 44$) are the independent fitting parameters to be optimized. So, the width of the Si_3N_4 overlayer can be given by

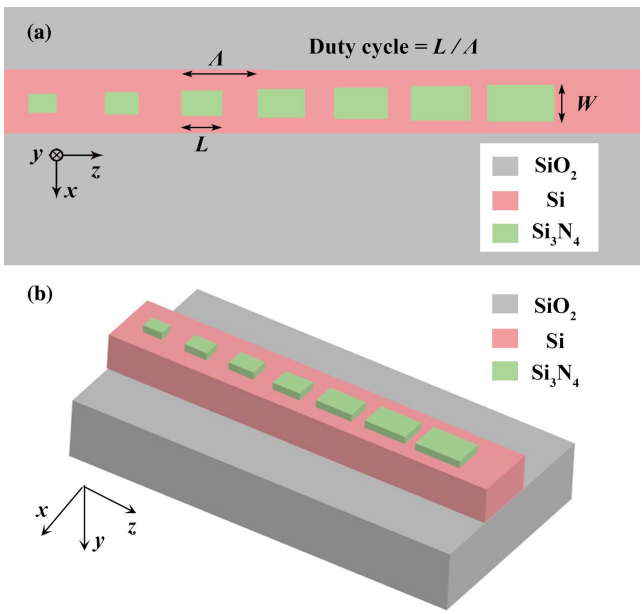

Fig. 1. (a) Partial schematic diagram of our proposed Si_3N_4/Si grating with a varying duty cycle and width of the Si_3N_4 overlayer. (b) Our proposed grating's 3D view without SiO_2 cladding.

$$W(z)=\begin{cases} g_1(S)\cdot W_{\mathrm{Si}}, & \Lambda(n-1)<z\le\Lambda(n-1)+\Lambda g_2(S), \\ 0, & \text{others}, \end{cases} \tag{2}$$

where $n=1+25(S-1),\ldots,25S$. Along the propagation direction, the z component of the coupling coefficient can be ignored, so it can be approximately expressed as

$$\kappa_{\mu\nu}(z)=\frac{j\omega\varepsilon_0}{4P_\xi}\int_0^{W(z)}\mathrm{d}x\int_0^{h_0}\mathrm{d}y(n^2-n_0^2)E_{\mu t}^{*}\cdot E_{\nu t}, \tag{3}$$

where P_ξ (ξ, a label indicating radiation modes) is the power spectral density. n and n_0 are the refractive index of Si_3N_4 and cladding medium, respectively. $E_{\mu t}$ and $E_{\nu t}$ are the transverse components of the electric field of the guided mode and radiation mode, respectively. Taking the coupling coefficients $\kappa_{\mu\nu}$ and $\kappa_{\nu\mu}$ as the core, a set of coupled-mode equations display the power transfer process between the guided mode and radiation mode. Actually, the continuity and infinity of the radiation mode derived from the semi-analytical model reduce the feasibility of mathematically solving its amplitude coefficients directly. We turn to investigate the attenuation efficiency of the guided mode to simplify solving the coupled-mode equations. The phase matching condition or quasi-phase matching condition stipulates that the guided mode can only be effectively coupled with some radiation modes with a special propagation constant β_ν. Hence, it can be approximately considered that the coupling coefficient $\kappa_{\mu\nu}$ no longer depends on the propagation constant β_ν. Under the semi-analytical model, the coupled-mode equations can be written as

$$\frac{\mathrm{d}A_m(z)}{\mathrm{d}z}\approx\sum_\nu\int a_\nu(z,\beta_\nu)\kappa_{m\nu}(z)\exp(-j\delta z)\mathrm{d}\beta_\nu, \tag{4a}$$

$$\frac{\mathrm{d}a_\nu(z,\beta_\nu)}{\mathrm{d}z}=\sum_m\kappa_{\nu m}(z)A_m(z)\exp(j\delta z), \tag{4b}$$

where $A_m(z)$ and $a_\nu(z)$ are the model amplitudes of the guided mode and radiation mode, respectively. $\delta=\beta_m-\beta_\nu$, where β_m is the propagation constant of the guided mode. The integral form of Eq. (4b) can be written as

$$a_\nu(z,\beta_\nu)=\int_0^z\sum_m\kappa_{\nu m}(z')A_m(z')\exp(j\delta z')\mathrm{d}z'. \tag{5}$$

In our design, it is assumed that the guided mode is the TE_{00} mode, so $m=1$. Then, substituting Eq. (5) into Eq. (4a), together with is $\kappa_{m\nu}=-\kappa_{\nu m}^{*}$, the attenuation of the guided mode can be expressed as

$$\frac{\mathrm{d}A_m(z)}{\mathrm{d}z}=-\pi\sum_\nu|\kappa_{m\nu}(z)|^2A_m(z). \tag{6}$$

The attenuation of the TE_{00} mode per unit length along the z direction can be given by

$$\frac{\mathrm{d}P_m(z)}{\mathrm{d}z}=-2\pi\sum_\nu|\kappa_{m\nu}(z)|^2|A_m(z)|^2, \tag{7}$$

where the right part contains all the power of the guided mode coupled to all radiation modes per unit length, that is, the emission profile. GA has excellent adaptive optimization global search capability[28], which is suitable for our tricky optimization problem without any prior knowledge to realize an approximate Gaussian emission profile along the grating emitter. We take the quantitative similarity between the calculated emission profile and a Gaussian model as the loss function.

3. Result and Analysis

The optimized width and duty cycle distribution of the Si_3N_4 overlayers in each grating period are plotted in Fig. 2(a) as the solid black line and the solid red line, respectively. Assuming that the amplitude of the normalized fundamental guided mode is 1 (a.u.), the corresponding optimized emission profile at the wavelength of 1550 nm along the 2.247 mm grating length is plotted in Fig. 2(b). The solid black line represents the calculation result, agreeing well with a fitted Gaussian curve, having the expected value $\mu=0.001$ and variance $\sigma^2=9\times10^{-8}$, plotted with the solid red line. Their quantitative similarity can be expressed using the following cross-correlation coefficient formula, where F_1 and F_2 represent our optimized distribution of the emission profile and the corresponding fitted Gaussian profile, respectively:

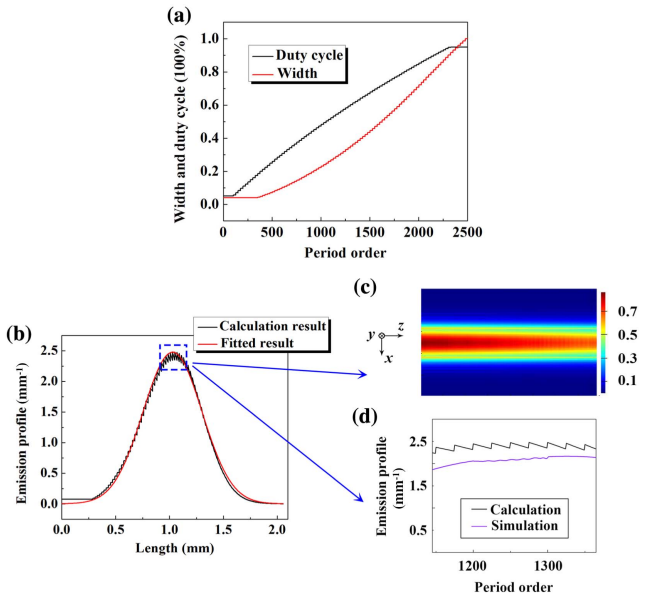

Fig. 2. (a) Optimized width and duty cycle distribution of the Si_3N_4 overlayer as a function of the grating period order. (b) The corresponding emission profile for our designed grating with a length of 2.247 mm at the wavelength of 1550 nm. (c) The major electric field distribution of the guided mode during the grating periods of 1145–1365. (d) The comparison of the calculated emission profile and the results simulated by FDTD in the same grating region.

$$C = \frac{\int_0^L F_1 \cdot F_2 \mathrm{d}z}{\sqrt{\int_0^L |F_1|^2 \mathrm{d}z} \cdot \sqrt{\int_0^L |F_2|^2 \mathrm{d}z}} = 0.9992, \tag{8}$$

where the integral variable z is the propagation distance of the light in the longitudinal direction, and L indicates the total propagation distance. The cross-correlation coefficient of 0.9992 strongly suggests that our designed grating has an emission profile nearly approaching an ideal Gaussian profile. The emission profile in the grating periods of 1145–1365 is investigated using a 3D FDTD method. The corresponding major electric field distribution of the guided mode is depicted in Fig. 2(c), and the calculated emission profile, shown in Fig. 2(d), approaches the results simulated by 3D FDTD, which further illustrates the effectiveness and accuracy of our design. Unfortunately, through the simulated result, the unidirectionality of our device only exceeds 46.2%, which can be improved by dual-layer grating misalignment[21].

At the wavelength of 1550 nm, the far-field beam profile for our proposed grating with the approximate Gaussian near-field emission intensity is shown in Fig. 3(a). The simulated FWHM beamwidth is as low as 0.026°, and the SSR is as high as 32.622 dB. Figure 3(b) illustrates the far-field intensity distribution for beam steering within the 1530–1570 nm wavelength range with a 5 nm step. A steering angle of 3.94° centered at 30° (working wavelength of 1550 nm) is achieved with approximately 0.1° per nanometer angular steering dispersion. Moreover, the far-field SSR for the 1530–1570 nm wavelength range is greater than 32 dB, suggesting that high-performance beam steering can be maintained during wavelength tuning.

In practice, deviations in fabricated dimensions of the Si_3N_4 overlayers from designed dimensions can lead to the radiation pattern change in our proposed grating antenna. To simulate the impact of fabrication errors as accurately as possible, we apply the Monte Carlo method to characterize the radiation fluctuations in the far field, assuming that the fabrication errors of the width and length (that is duty cycle) of the Si_3N_4 overlayer satisfy the Gaussian random distribution with mean value $\mu = 0$. Table 1 presents the averaged far-field SSR with the standard deviation σ varying from 10 nm to 60 nm, and Fig. 4 shows the error maps at $\sigma = 30$ nm, 40 nm, 50 nm, and 60 nm, respectively. The results show that the grating antenna can still maintain good performance with reasonable fabrication errors, e.g., σ below 30 nm, which is a quite exaggerated error for any state-of-the-art CMOS photonics foundry. Hence, our design could hold considerable merit and value in developing practical large aperture solid-state phase arrays.

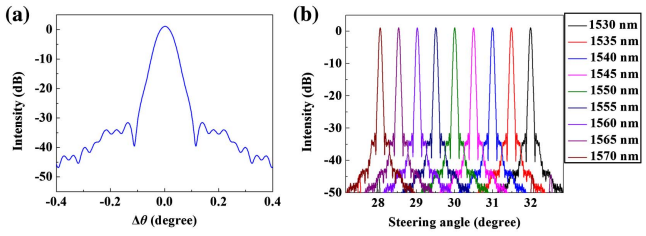

Fig. 3. (a) Far-field intensity distribution for our proposed grating at the 1550 nm wavelength. (b) Far-field intensity distribution for beam steering within 1530–1570 nm wavelength range with a 5 nm step.

Table 1. Effect of Changes in Si_3N_4 Overlayer Width and Length on the SSR of Our Proposed Grating.

Monte-Carlo Model		
μ	σ (nm)	Average SSR (dB)
0	10	32.227
	20	30.766
	30	29.110
	40	26.130
	50	17.707
	60	15.379

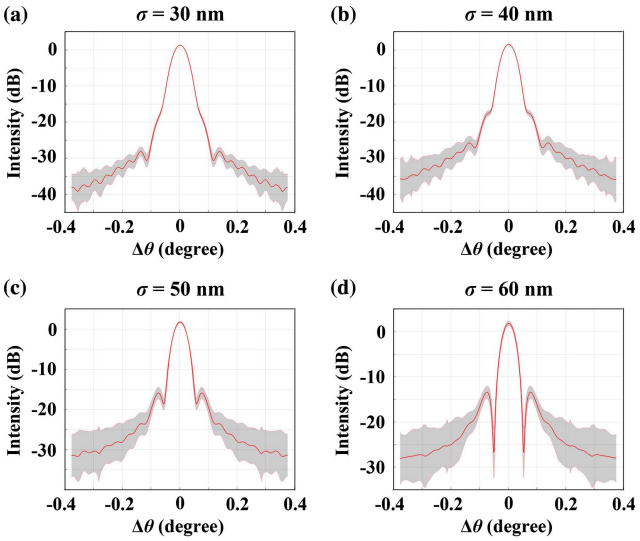

Fig. 4. Error maps of our proposed grating when σ = 30–60 nm, respectively. The red line indicates the average intensity, and the gray area represents the standard deviation of the intensity error at each point.

4. Conclusion

In conclusion, we have proposed a practical design of a Si_3N_4 overlayer assisted Si grating emitter with an approximate Gaussian emission profile over > 2 mm length, which has a narrow angular FWHM of 0.026° and a large far-field SSR of 32.622 dB. The theory clearly reveals the general way to design a grating with a special emission profile by using CMT and GA. Further analysis shows that our emitter can also function well with almost undeteriorated angular divergence and SSR performance for the wavelength range from 1530 nm to 1570 nm,

while achieving a longitudinal steering angle of about 3.94°. Our theoretical analysis indicates that our design is robust to practical fabrication errors for the width and length of the Si_3N_4 overlayer. We believe that the high-performance solid-state lidar systems can benefit from our demonstrated device.

Appendix A: Radiation Mode

As shown in Fig. 5, in the upper half of coordinate space, visualizing that a plane wave from infinity impinges onto the surface of the ideal Si waveguide, a portion of this wave is scattered (or reflected) at the core boundary, and the remaining wave is refracted into the waveguide. The total field outside the Si core consists of the incoming field and the response field of the boundary to it. The resulting radiation field (e.g., the total field) is the eigen-solutions of Maxwell's equations under specific boundary conditions. The propagation constant q of the radiation mode forms a continuum because it is related to the incident direction of the incoming field, which indicates that radiation modes are also continuous in the q space. Confusion may arise in the previous discussion of setting up the theoretical model, e.g., the radiation mode in our model is a standing wave, which someone may confuse with the fact that the radiation field is an outgoing traveling wave. The explanation is that the guided mode in the core of the perturbed waveguide would excite a series of infinite continuous radiation modes, in which the incoming fields are eliminated by destructive interference[25], while the response fields superimpose themselves into an outgoing traveling wave.

In the internal region of the Si core, the transverse propagation constant can be defined as $\eta = (n_g^2k^2 - \beta_v^2)^{1/2}$, and, in the external region, $\rho = (n_c^2k^2 - \beta_v^2)^{1/2}$, where n_gk and n_ck are the wavenumbers in the Si waveguide and SiO_2 cladding, respectively, and β_v $(-n_ck \le \beta_v \le n_ck)$ is the longitudinal propagation constant of radiation mode v in the SiO_2 cladding. In the radiation model, the longitudinal components of electric and magnetic fields can be expanded in terms of cylindrical harmonic functions, which are expressed as[26,27]

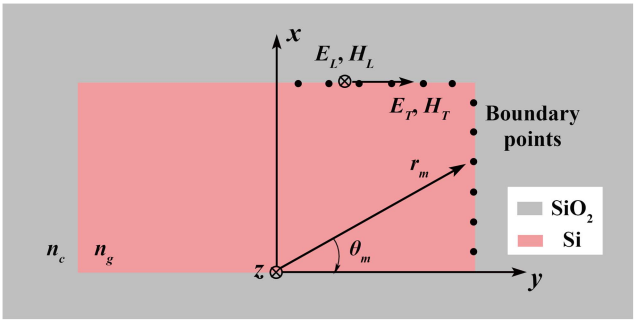

Fig. 5. Profile diagram of a rectangular Si waveguide surrounded by SiO_2. n_g and n_c represent the refractive index of the waveguide and the cladding, respectively. E_L and H_L are the longitudinal (z-axis) parts of the electric field and magnitude field located at the boundary. E_T and H_T are the transverse components. The discrete boundary grid points are represented by (r_m, θ_m).

$$\begin{cases} E_z^{\text{in}}(r,\theta) = \sum_{m=0}^{\infty} A_m J_m(\eta r)\sin(m\theta+\varphi) \\ H_z^{\text{in}}(r,\theta) = \sum_{m=0}^{\infty} B_m J_m(\eta r)\cos(m\theta+\varphi) \end{cases} \tag{A1}$$

in the internal region, and

$$\begin{cases} E_z^{\text{ex}}(r,\theta) = \sum_{m=0}^{\infty} C_m H_m^{(1)}(\rho r)\sin(m\theta+\varphi) \\ \qquad + P_N J_N(\rho r)\sin(N\theta+\varphi) \\ H_z^{\text{ex}}(r,\theta) = \sum_{m=0}^{\infty} D_m H_m^{(1)}(\rho r)\cos(m\theta+\varphi) \\ \qquad + Q_N J_N(\rho r)\cos(N\theta+\varphi) \end{cases} \tag{A2}$$

in the external region. Here, the terms J_m and $H_m^{(1)}$ are the mth-order Bessel functions and Hankel functions of the first kind, respectively. Hankel functions of the first kind possess the characteristics of an actual outgoing traveling wave, solving the seeming paradox. The coefficients P_N and Q_N, satisfying $P_N \cdot Q_N = 0$, represent the magnitudes of the incoming field and can directly determine the power spectral density P_ξ (ξ, a label indicating radiation modes) for the normalization of radiation modes. When $P_N = 0$, $Q_N \neq 0$, the incoming field exhibits E polarization, and, when $P_N \neq 0$, $Q_N = 0$, it shows H polarization. Furthermore, the parity of the order N and m, together with the phase φ ($\varphi = 0$ or $\pi/2$) factor, identifies the symmetry of a certain radiation mode. The selection rules of these parameters are listed in Table 1. To some extent, the radiation modes can thus be defined as resulting from the response of the waveguide to an incoming field possessing a given polarization and symmetry.

The tangential components (represented by E_T and H_T) and longitudinal components (represented by E_L and H_L) of the radiation model must be continuous at the boundary of the Si waveguide. Deriving from the symmetry of the fields, we choose the core boundary in the first quadrant in Fig. 5 and discretize it into M boundary points (r_m,θ_m), where r_m is the length from the origin to a boundary point and $\theta_m = (\pi/2)\cdot(m-0.5)/M$ $(m = 1, n, M)$. Furthermore, a series of cylindrical harmonics in Eqs. (A1) and (A2) must be appropriately truncated, which ensures that the extension coefficients A_m, B_m, C_m, and D_m occupy the unique solution. Combining these matching equations, we finally get a $4M \times 4M$ matrix equation system about expansion coefficients (see Ref. [27] for details). In the semi-analytical radiation model, high-order cylindrical harmonics hardly contribute to the longitudinal components of the radiation field. Therefore, when M is large enough, the truncated Eqs. (A1) and (A2) can also ensure high calculation accuracy. The real z components of the electric field of different radiation modes are depicted in Fig. 6, with N taking values in the range of 1–4, which meets the symmetry requirements of the radiation mode shown in Table 2.

Given the longitudinal propagation constant β_v, the coefficient N, the phase factor φ, and the polarization of the incoming field, the total radiation field of an ideal Si waveguide is then given by

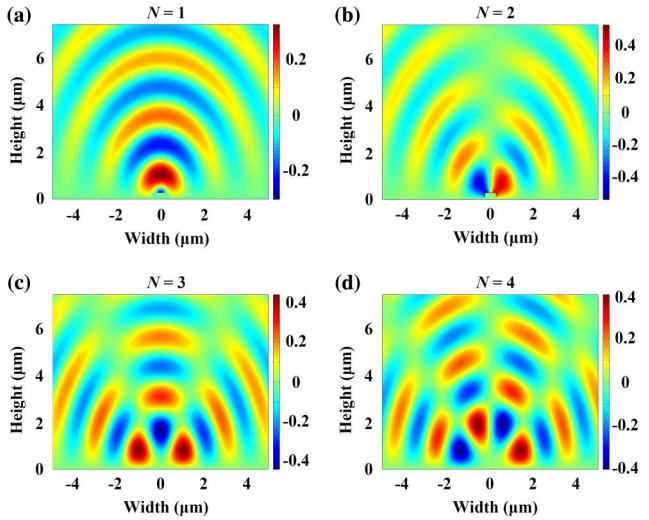

Fig. 6. (a)–(d) Distribution of the z component of the electric field of the radiation mode outside the waveguide, corresponding to $N = 1$–4, respectively. We assume that the incident wavelength $\lambda = 1550$ nm, the longitudinal propagation constant $\beta_\nu = 2.926\ \mu m^{-1}$, the phase factor $\varphi = 0$, and the incoming polarization is H polarization.

Table 2. Selection Rules of the Parameter N, m, and φ, and the Corresponding Symmetries of Incoming Fields[a].

N	φ	m (E)	m (H)	Symmetry
Odd (> 0)	0	Odd	Odd	Symmetric
	$\pi/2$	Odd	Odd	Anti-symmetric
Even (> 0)	0	Even	Even	Anti-symmetric
	$\pi/2$	Even	Even	Symmetric
0	0	Even	Even	Anti-symmetric
	$\pi/2$	Even	Even	Symmetric

[a]When $N = 0$ and $\varphi = 0$, incident wave is E polarization, so $Q_N \neq 0$. When $N = 0$ and $\varphi = \pi/2$, $P_N \neq 0$.

$$\begin{cases} E_{\text{rad}} = \sum_j \int_0^{kn_c} a_j(\beta_\nu) e_j(x,y,\beta_\nu) \exp(\beta_\nu z) \mathrm{d}\beta_\nu \\ H_{\text{rad}} = \sum_j \int_0^{kn_c} a_j(\beta_\nu) h_j(x,y,\beta_\nu) \exp(\beta_\nu z) \mathrm{d}\beta_\nu \end{cases}, \tag{A3}$$

where a_j is the model amplitude. The integration indicates that the radiation mode is continuous in terms of the propagation constant, and the summation shows that the radiation modes are discrete in terms of spatial symmetry.

Acknowledgement

This work was supported by the Shanghai Municipal Science and Technology Major Project (No. 2017SHZDZX03).

References

1. C. V. Poulton, A. Yaacobi, D. B. Cole, M. J. Byrd, M. Raval, D. Vermeulen, and M. R. Watts, "Coherent solid-state LIDAR with silicon photonic optical phased arrays," Opt. Lett. **42**, 4091 (2017).
2. C. V. Poulton, M. J. Byrd, P. Russo, E. Timurdogan, M. Khandaker, D. Vermeulen, and M. R. Watts, "Long-range LiDAR and free-space data communication with high-performance optical phased arrays," IEEE J. Sel. Top. Quantum Electron. **25**, 7700108 (2019).
3. C. V. Poulton, M. J. Byrd, E. Timurdogan, P. Russo, D. Vermeulen, and M. R. Watts, "Optical phased arrays for integrated beam steering," in *IEEE 15th International Conference on Group IV Photonics (GFP)* (IEEE, 2018).
4. C.-S. Im, B. Bhandari, K.-P. Lee, S.-M. Kim, M.-C. Oh, and S.-S. Lee, "Silicon nitride optical phased array based on a grating antenna enabling wavelength-tuned beam steering," Opt. Express **28**, 3270 (2020).
5. T. Raj, F. H. Hashim, A. B. Huddin, M. F. Ibrahim, and A. Hussain, "A survey on LiDAR scanning mechanisms," Electronics **9**, 741 (2020).
6. P. F. McManamon, P. Banks, J. Beck, D. G. Fried, A. S. Huntington, and E. A. Watson, "Comparison of flash lidar detector options," Opt. Eng. **56**, 031223 (2017).
7. D. N. Hutchison, J. Sun, J. K. Doylend, R. Kumar, J. Heck, W. Kim, C. T. Phare, A. Feshali, and H. Rong, "High-resolution aliasing-free optical beam steering," Optica **3**, 887 (2016).
8. D. Kwong, A. Hosseini, J. Covey, Y. Zhang, X. Xu, H. Subbaraman, and R. T. Chen, "On-chip silicon optical phased array for two-dimensional beam steering," Opt. Lett. **39**, 941 (2014).
9. S. A. Miller, Y.-C. Chang, C. T. Phare, M. C. Shin, M. Zadka, S. P. Roberts, B. Stern, X. Ji, A. Mohanty, O. A. Jimenez Gordillo, U. D. Dave, and M. Lipson, "Large-scale optical phased array using a low-power multi-pass silicon photonic platform," Optica **7**, 3 (2020).
10. J. Sun, E. Timurdogan, A. Yaacobi, E. S. Hosseini, and M. R. Watts, "Large-scale nanophotonic phased array," Nature **493**, 195 (2013).
11. L. Wang, Z. Chen, H. Wang, A. Liu, P. Wang, T. Lin, X. Liu, and H. Lv, "Design of a low-crosstalk half-wavelength pitch nano-structured silicon waveguide array," Opt. Lett. **44**, 3266 (2019).
12. S. Jahani, S. Kim, J. Atkinson, J. C. Wirth, F. Kalhor, A. Al Noman, W. D. Newman, P. Shekhar, K. Han, V. Van, R. G. Decorby, L. Chrostowski, M. Qi, and Z. Jacob, "Controlling evanescent waves using silicon photonic all-dielectric metamaterials for dense integration," Nat. Commun. **9**, 1893 (2018).
13. S. Jahani and Z. Jacob, "Transparent subdiffraction optics: nanoscale light confinement without metal," Optica **1**, 96 (2014).
14. D. Kwong, A. Hosseini, J. Covey, X. Xu, Y. Zhang, S. Chakravarty, and R. T. Chen, "Corrugated waveguide-based optical phased array with crosstalk suppression," IEEE Photon. Technol. Lett. **26**, 991 (2014).
15. B. Shen, R. Polson, and R. Menon, "Increasing the density of passive photonic-integrated circuits via nanophotonic cloaking," Nat. Commun. **7**, 13126 (2016).
16. L. Zhang, Y. Li, Y. Hou, Y. Wang, M. Tao, B. Chen, Q. Na, Y. Li, Z. Zhi, X. Liu, X. Li, F. Gao, X. Luo, G.-Q. Lo, and J. Song, "Investigation and demonstration of a high-power handling and large-range steering optical phased array chip," Opt. Express **29**, 29755 (2021).
17. W. Xie, T. Komljenovic, J. Huang, M. Tran, M. Davenport, A. Torres, P. Pintus, and J. Bowers, "Heterogeneous silicon photonics sensing for autonomous cars [Invited]," Opt. Express **27**, 3642 (2019).
18. J. C. Hulme, J. K. Doylend, M. J. R. Heck, J. D. Peters, M. L. Davenport, J. T. Bovington, L. A. Coldren, and J. E. Bowers, "Fully integrated hybrid silicon two dimensional beam scanner," Opt. Express **23**, 5861 (2015).
19. M. Zadka, Y.-C. Chang, A. Mohanty, C. T. Phare, S. P. Roberts, and M. Lipson, "On-chip platform for a phased array with minimal beam divergence and wide field-of-view," Opt. Express **26**, 2528 (2018).
20. M. Raval, C. V. Poulton, and M. R. Watts, "Unidirectional waveguide grating antennas for nanophotonic phased arrays," in *Conference on Lasers and Electro-Optics (CLEO)* (IEEE, 2017).
21. B. Chen, Y. Li, L. Zhang, Y. Li, X. Liu, M. Tao, Y. Hou, H. Tang, Z. Zhi, F. Gao, X. Luo, G. Lo, and J. Song, "Unidirectional large-scale waveguide grating with uniform radiation for optical phased array," Opt. Express **29**, 20995 (2021).

22. S. Katoch, S. S. Chauhan, and V. Kumar, "A review on genetic algorithm: past, present, and future" Multimed. Tools Appl. **80**, 8091 (2021).
23. Y. Song, F. Wang, and X. Chen, "An improved genetic algorithm for numerical function optimization," Appl. Intell. **49**, 1880 (2019).
24. A. Arabali, M. Ghofrani, M. Etezadi-Amoli, M. S. Fadali, and Y. Baghzouz, "Genetic-algorithm-based optimization approach for energy management," IEEE Trans. Power Deliv. **28**, 162 (2013).
25. D. Marcuse, *Theory of Dielectric Optical Waveguides*, 2nd ed. (Harcourt Brace Jovanovich, 1991).
26. A. W. Snyder and R. A. Sammut, "Radiation modes of optical waveguides," Electron. Lett. **15**, 4 (1979).
27. C. G. Poulton, C. Koos, M. Fujii, A. Pfrang, T. Schimmel, J. Leuthold, and W. Freude, "Radiation modes and roughness loss in high index-contrast waveguides," IEEE J. Sel. Top. Quantum Electron. **12**, 1306 (2006).
28. L. Ma, J. Li, Z. Liu, Y. Zhang, N. Zhang, S. Zheng, and C. Lu, "Intelligent algorithms: new avenues for designing nanophotonic devices [Invited]," Chin. Opt. Lett. **19**, 011301 (2021).